

Formation of Dense and High-Aspect-Ratio Iron Oxide Nanowires by Water-Vapor-Assisted Thermal Oxidation and their Cr(VI) Adsorption Properties

Faisal Budiman

Telkom University

Wai Kian Tan (✉ tan@las.tut.ac.jp)

Toyohashi University of Technology: Toyohashi Gijutsu Kagaku Daigaku

Go Kawamura

Toyohashi University of Technology: Toyohashi Gijutsu Kagaku Daigaku

Hiroyuki Muto

Toyohashi University of Technology: Toyohashi Gijutsu Kagaku Daigaku

Atsunori Matsuda

Toyohashi University of Technology: Toyohashi Gijutsu Kagaku Daigaku

Khairunisak Abdul Razak

Universiti Sains Malaysia

ZAINOVIA LOCKMAN

Universiti Sains Malaysia - Engineering Campus Seri Ampangan: Universiti Sains Malaysia - Kampus Kejuruteraan Seri Ampangan

Research Article

Keywords: Hexavalent Chromium, Adsorption, Hematite, Nanowires, Thermal Oxidation, Water Vapor

Posted Date: June 29th, 2021

DOI: <https://doi.org/10.21203/rs.3.rs-598647/v1>

License: © ⓘ This work is licensed under a Creative Commons Attribution 4.0 International License.

[Read Full License](#)

Formation of Dense and High-Aspect-Ratio Iron Oxide Nanowires by Water-Vapor-Assisted Thermal Oxidation and their Cr(VI) Adsorption Properties

Faisal Budiman^{1,2}, Wai Kian Tan^{3*}, Go Kawamura⁴, Hiroyuki Muto^{3,4}, Atsunori Matsuda⁴, Khairunisak Abdul Razak¹ and Zainovia Lockman^{1*}

¹Green Electronic Nanomaterials Group, School of Materials and Mineral Resources Engineering, Engineering Campus, Universiti Sains Malaysia, 14300 Nibong Tebal, Penang, Malaysia

²Department of Electrical Engineering, School of Electrical Engineering, Telkom University, Jl. Telekomunikasi No. 1 Bandung 40257, Indonesia

³Institute of Liberal Arts & Sciences, Toyohashi University of Technology, Toyohashi, Aichi, 441-8580, Japan

⁴Department of Electrical and Electronic Information Engineering, Toyohashi University of Technology, Toyohashi, Aichi 441-8580, Japan

*E-mail: zainovia@usm.my

Abstract

In this work, highly crystalline and high aspect ratio α -Fe₂O₃ nanowire (NWs) were successfully produced by thermal oxidation of iron in water vapor at 800 °C. The process was done for 2 h and the NWs were found to be covering the foil uniformly unlike when the oxidation environment was dry whereby the NWs formed were shorted and rather dispersed. The formation of NWs was proposed to be due to a stress-driven surface diffusion during thermal oxidation process. When oxidation was done at 700 °C, we observed coral-like nanostructures. The α -Fe₂O₃ NWs were then used as adsorbent to remove Cr(VI) from stimulated wastewater. Removal efficiency of 97% in a 225 mg/L Cr(VI) solution was observed indicating very fast removal of Cr(VI) in the presence of the NWs. The kinetic characteristic of the adsorption was fitted to a pseudo-second-order kinetic model, and isothermal studies indicated that the α -Fe₂O₃ NWs exhibited an adsorption capacity of 66.26 mg/g.

Keywords: Hexavalent Chromium, Adsorption, Hematite, Nanowires, Thermal Oxidation, Water Vapor

1. Introduction

Chromium has oxidation states from (II) to (VI), but is most stable in its trivalent (III) [Cr(III)] and hexavalent (VI) [Cr(VI)] forms; however, Cr(VI) rarely occurs naturally and is typically manufactured. Unlike Cr(III), Cr(VI) is toxic and carcinogenic (Guertin et al. 2016; Rahman and Singh 2019): excessive inhalation of Cr(VI) can lead to lung cancer (Lin et al. 2019); direct skin contact with it may result in dermatitis (Lejding et al. 2020); and when ingested, it can cause organ damage (Yu et al. 2020). Cr(VI) compounds are, nonetheless, extremely important for electroplating, steel manufacturing, leather tanning, and textile production (Rosli et al. 2021). Inevitably, wastewater from these processes contains large amounts of Cr(VI), and, unless properly treated, it can enter surface waters, causing harm to aquatic life and possibly entering the food chain. The World Health Organization has recommended that Cr(VI) concentrations in water should not exceed 0.05 mg/L (WHO, 2011); therefore, total removal of Cr(VI) from industrial wastewater is crucial to preventing surface water concentrations exceeding this level.

40 There are several accepted methods for removing Cr(VI), which typically exists as highly soluble and toxic
41 chromate anions (HCrO_4^- or $\text{Cr}_2\text{O}_7^{2-}$), from industrial wastewater: photocatalytic reduction (Rosli et al. 2021; Gao
42 et al. 2020; Bashirov et al. 2020), chemical precipitation (Xie et al. 2017), electrokinetic remediation (Zheng et
43 al. 2020), membrane filtration (Abdullah et al. 2019), and adsorption (Zhang et al. 2020; Rasheed et al. 2020).
44 Among these methods, adsorption is especially appealing, as it is very effective at removing even minute amounts
45 of Cr(VI) (Kumar et al. 2019). The adsorption process requires a solid surface (i.e., adsorbent) with a large surface
46 area for the species to be adsorbed (i.e., adsorbate) to attach to, either by physical or chemical processes.
47 Nanostructured materials present themselves as attractive large-surface-area adsorbents for this purpose, of which
48 one-dimensional nanostructures, such as nanowires (NWs), are particularly effective.

49 Iron oxide is a compound material, largely found as hematite ($\alpha\text{-Fe}_2\text{O}_3$), magnetite (Fe_3O_4), wüstite (Fe_{1-x}O), and maghemite ($\gamma\text{-Fe}_2\text{O}_3$) (Cornell and Schwertmann 2003), which has attracted attention as an adsorbent
50 due to its ability to remove various types of heavy-metal ions (Bahmani et al. 2019; Fayazi et al. 2019; Sruthi et
51 al. 2018; Khan et al. 2020). Recent studies have demonstrated that $\alpha\text{-Fe}_2\text{O}_3$ has a high adsorption capability, which
52 occurs through a chemisorption process involving the hydroxyl group on its surface (Singaraj et al. 2019). Ren et
53 al. investigated using $\alpha\text{-Fe}_2\text{O}_3$ in fibrous form for Cr(VI) ion removal and reported that the porous fiber-like
54 morphology of $\alpha\text{-Fe}_2\text{O}_3$ exhibited excellent adsorption of Cr(VI) from water, with rapid adsorption kinetics, high
55 adsorption capacity, and good reusability (Ren et al. 2013). Kumar et al. used magnetic iron oxide nanoparticles
56 for Cr(VI) removal and obtained an adsorption capacity of 1,052.63 mg/g (Kumar et al. 2019). In view of these
57 results, we attempted to prepare $\alpha\text{-Fe}_2\text{O}_3$ NWs through thermal oxidation of iron foils and investigated the
58 sample's ability to remove Cr(VI) from aqueous solutions.
59

60 Thermal oxidation can be used to produce thin-film oxides composed of NWs (Tan et al. 2011). Although
61 there are various other ways of producing $\alpha\text{-Fe}_2\text{O}_3$ NWs, such as electrospinning (Deng et al. 2018; Ponti et al. 2020),
62 hydrothermal (Sun et al. 2020), and nanocasting methods (Azeez et al. 2021), which produce NWs with a uniform
63 diameter and length, they are known to be time consuming, and post-annealing treatments are required for
64 crystalline oxide formation. Thermal oxidation presents a simpler approach to forming surface oxide layers, and,
65 through careful control of the oxidation parameters, e.g., oxidation temperature (Rahmat et al. 2018a; Rahmat et
66 al. 2018b; Srivastava et al. 2016; Budiman et al. 2016), unique nanostructures can be produced. Apart from
67 temperature, oxidation time and environment also affect the growth of NWs (Rahmat et al. 2020). Our previous
68 work explored the formation of iron oxide NWs by thermal oxidation in water-vapor-assisted conditions (Rahmat
69 et al. 2018b; Budiman et al. 2016). The presence of water vapor during oxidation induced more densely packed
70 nanostructures with a uniform distribution compared with those under dry-air conditions; however, this work was
71 performed at lower temperatures (400°C–500°C). When iron is oxidized at high temperatures, it grows an oxide
72 scale containing multilayered oxides, which are markedly different to the oxide phases formed below 570°C (Yu
73 et al. 2003; Aquino et al. 2020); therefore, investigating these high-temperature oxidations further may result in
74 novel and potentially useful nanostructures for various applications, including adsorption.

75 Our previous work on the synthesis of iron oxide NWs using thermal oxidation focused on a low-temperature
76 oxidation regime (Budiman et al. 2016). In this study, we investigated the formation of iron oxide nanostructures
77 by thermal oxidation under water-vapor-assisted conditions at high temperatures (i.e., 700°C and 800°C) to assess
78 the Cr(VI) removal capability of the samples. This study makes a number of important contributions relating to
79 the growth of iron oxide NWs at temperatures $> 570^\circ\text{C}$ under water vapor, proposing a mechanism of the NW

80 formation and exploring the Cr(VI) adsorption properties of the NWs, which were also evaluated by kinetic and
81 equilibrium studies.

82

83 2. Experimental procedure

84 The 1 × 1 cm iron foils (99.9%, Nilaco Corporation) were polished with a 2,000-grit silicon carbide paper,
85 ultrasonically cleaned in acetone, rinsed using deionized water, and then dried. Then, they were placed in an
86 alumina crucible and positioned in the hot zone of a horizontal furnace. The furnace was progressively heated by
87 5°C /min until the desired oxidation temperature was reached, which was either 700°C or 800°C. Once this
88 temperature was reached, the furnace was purged with water vapor generated using a nebulizer (Omron NE-C801).
89 The evolution of the surface oxide was monitored using a field-emission electron microscope (FESEM) (Zeiss
90 Supra 35 VP), and higher magnification images were obtained using a high-resolution transmission electron
91 microscope (HR-TEM) (Tecnai G² 20 S-TWIN). Crystal structures were examined by taking X-ray diffraction
92 (XRD) patterns (Bruker D8 Advance diffractometer) with a Cu K_α radiation source (λ = 0.154 nm)). A Raman
93 spectrometer (Renishaw RL633) was used for phase identification, and an X-ray photoelectron spectrophotometer
94 (XPS) (Kratos Axis Ultra XPS Spectroscopy) with an Al X-ray radiation source was used for surface and
95 elemental analysis.

96 To evaluate the Cr(VI) removal ability of the nanostructures, oxidized iron with α-Fe₂O₃ NWs was placed
97 in Cr(VI) solutions of various concentrations between 225–300 mg/L. The pH of the solutions was adjusted to pH
98 2 by adding H₂SO₄. The assessment of Cr(VI) content was performed using a diphenyl-carbazide (DPC)
99 colorimetry method. DPC solution was prepared by diluting 0.25 g of 1,5-diphenylcarbazide in 50 ml acetone,
100 and a droplet was added into the Cr(VI) solutions. A colour change in the solution to purple indicated the existence
101 of Cr(VI). UV-Visible (UV-Vis) measurements were taken with a UV-Vis spectrophotometer (Perkin Elmer
102 Lambda 35), and absorption values were recorded at a wavelength of 540 nm to detect Cr(VI) (Onchoke et al.
103 2016). The adsorption study was divided into two parts: equilibrium and kinetic. First, 50 ml solutions of Cr(VI)
104 with concentrations ranging from 225 to 300 mg/L were prepared. The α-Fe₂O₃ NWs were then immersed in the
105 Cr(VI) solution. During this adsorption process, bubbles, which were supplied by an air pump (Super X Classica)
106 with an output of 250 L/h, were used for stirring the Cr(VI) solution. The amount of Cr(VI) adsorbed at the
107 equilibrium condition (q_e) was calculated using Eq. 1:

$$108 \quad q_e = \frac{(C_o - C_e).V}{m}, \quad (1)$$

109 where C_o and C_e are the initial and equilibrium concentrations of Cr(VI) (mg/L), respectively; V is the volume of
110 solution used (L); and m is the mass of the adsorbent (g). For the kinetic study, the amount of Cr(VI) adsorbed at
111 time t (q_t) was calculated using Eq. 2:

$$112 \quad q_t = \frac{(C_o - C_t).V}{m}, \quad (2)$$

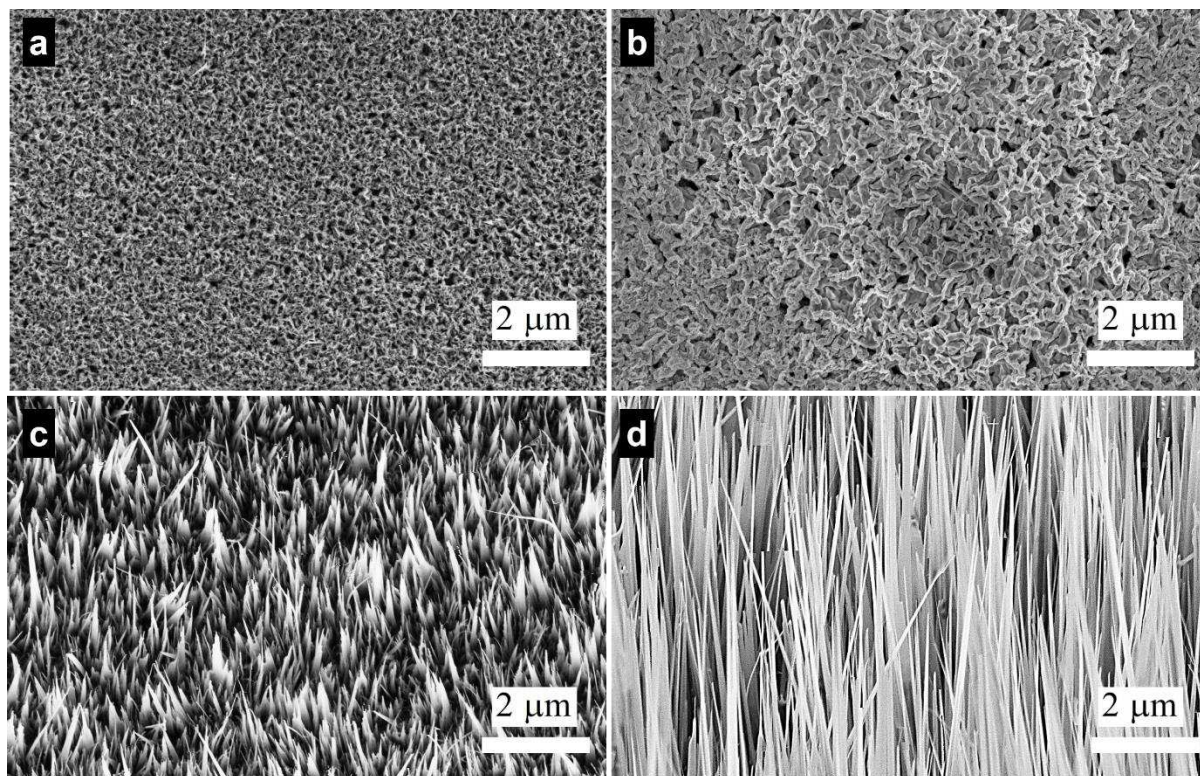
113 where C_t is the concentration of Cr(VI) at time t .

114

115 3. Results and discussion

116 3.1 Morphology observations

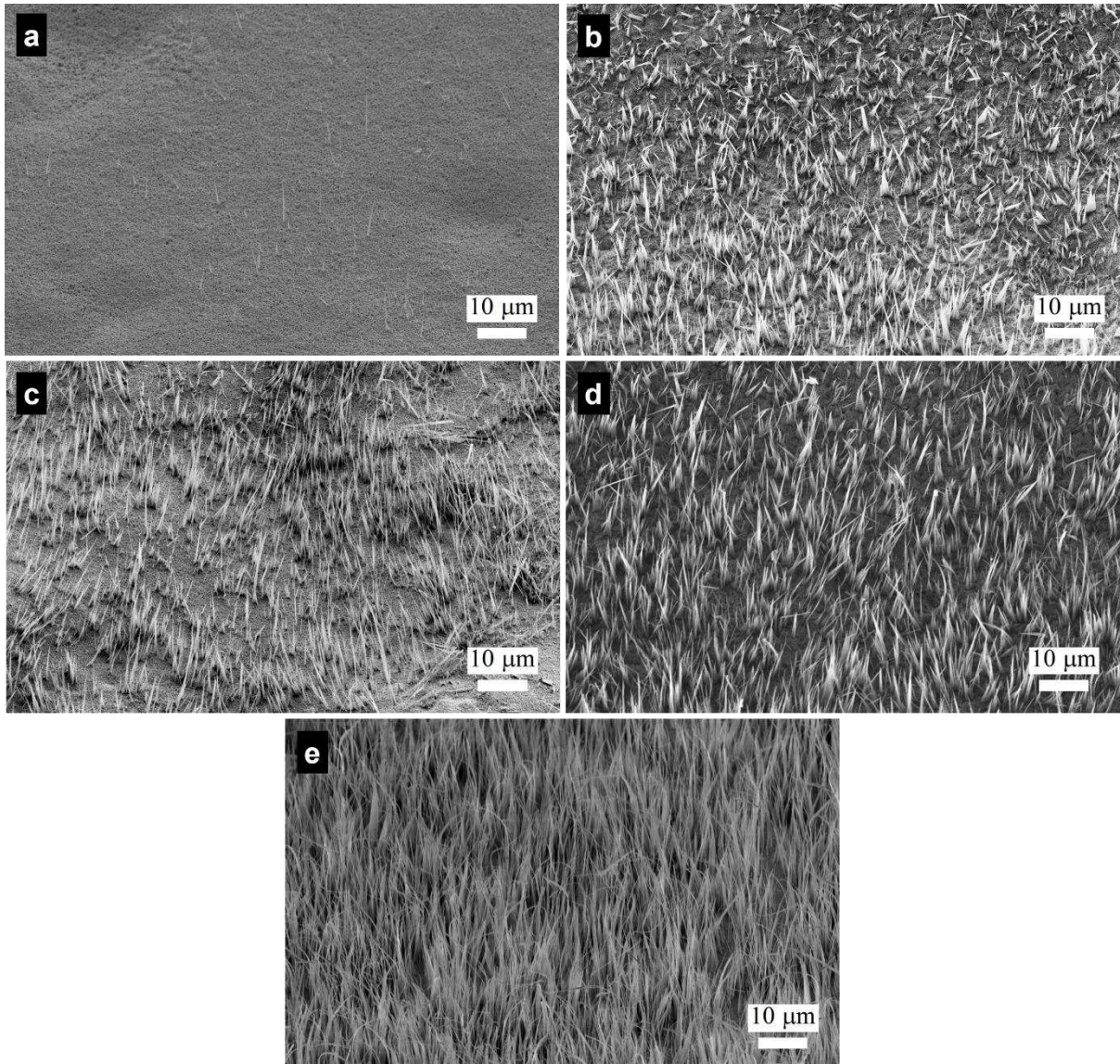
117 FESEM images of the surface morphologies of the foils oxidized in dry air and water vapor are presented
118 Figs. 1 (a) and (b), respectively. At 700°C, the surface oxidization exhibited a coral-like structure, which was
119 larger on the water-vapor-oxidized sample than on the air-oxidized sample. Micrographs of the foils oxidized at
120 800°C in dry air and water vapor are presented in Figs. 1 (c) and (d), respectively, and they show that the NWs
121 formed on these foils were finer and longer (up to 20 μm) when oxidized in water vapor. This demonstrated that
122 water-vapor-assisted thermal oxidation strongly influenced the aspect ratio of the NWs.
123
124



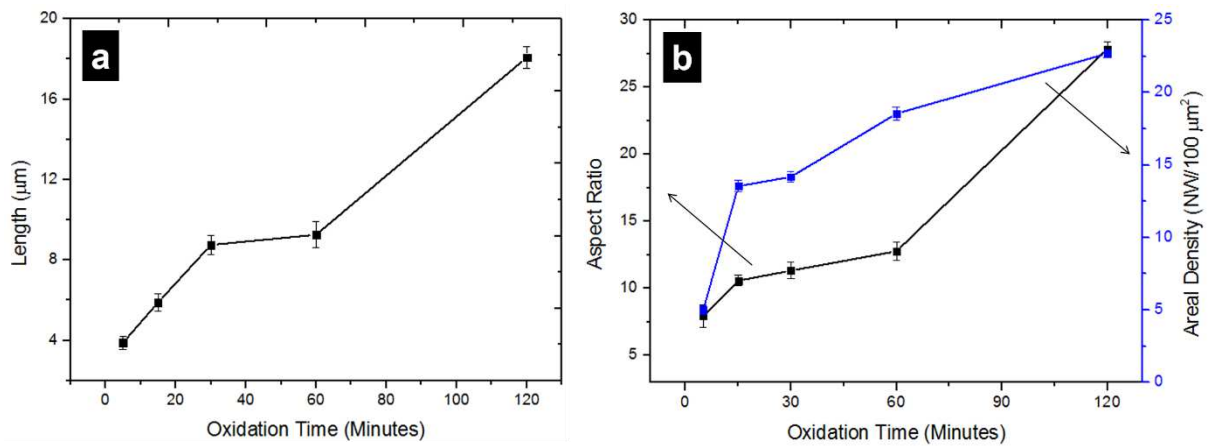
125
126 Fig. 1. FESEM images of iron foils oxidized for 2 h in (a) 700 °C air, (b) 700 °C water vapor, (c) 800 °C air,
127 and (d) 800 °C water vapor.

128
129 To further investigate the effect of water vapor on the growth of the NWs, various oxidation durations were
130 applied at 800°C, and the resulting surface morphologies are illustrated in Fig. 2. Interestingly, the NWs were
131 formed after only 5 min of oxidation, as illustrated in Fig. 2 (a), but the areal density was initially low with only
132 sparse NWs formed on the foil surface. Here areal density was defined as the number of NWs per measured area
133 in an FESEM image. Extending the oxidation time to 15, 30, and 60 min increased the areal density of the NWs,
134 as illustrated in Figs. 2 (b–d), respectively, and oxidation for 120 min resulted in the formation of a dense,
135 homogenous NW surface, as illustrated in Fig. 2 (e); therefore, we concluded that both the length and diameter of
136 the NWs increased with increasing oxidation time. A summary of the morphological observations at 800°C,
137 including those of the length, aspect ratio, and areal density as a function of oxidation time, is presented in Fig. 3.
138 These results indicate that controlled formation of $\alpha\text{-Fe}_2\text{O}_3$ NWs can be achieved by controlling the oxidation time
139 during water-vapor-assisted thermal oxidation.

140



141
 142 Fig. 2. FESEM images of the oxidized iron at 800°C in water vapor for (a) 5, (b) 15, (c) 30, (d) 60, and (e)
 143 120 min.
 144

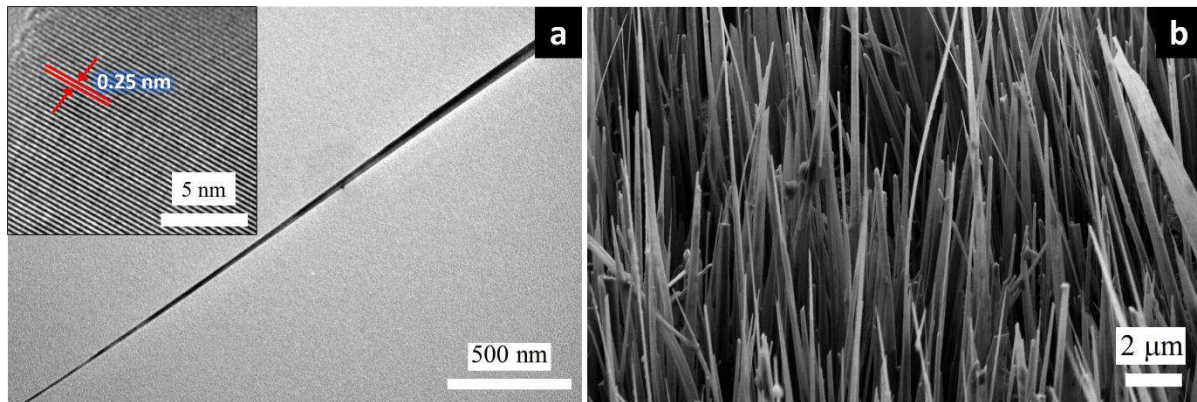


145
 146 Fig. 3. Quantitative analysis of the (a) length, (b) aspect ratio, and (c) areal density of the iron foils oxidized
 147 at 800°C for 5–120 min.

148

149 To gain an insight into the crystallinity of the NWs, we performed HR-TEM observations of a single α -Fe₂O₃ NW
150 obtained through water-vapor-assisted thermal oxidation at 800°C for 2 h. The subsequent HR-TEM image is
151 presented Fig. 4 (a), which indicates that the diameters of the bottom and tip of the nanowire were approximately
152 60 and 5 nm, respectively. The image also shows that the measured d-spacing was approximately 0.25 nm, which
153 is in accordance with the (110) plane of α -Fe₂O₃. The tapered structure of the NWs was confirmed by the FESEM
154 image in Fig. 4 (b).

155



156

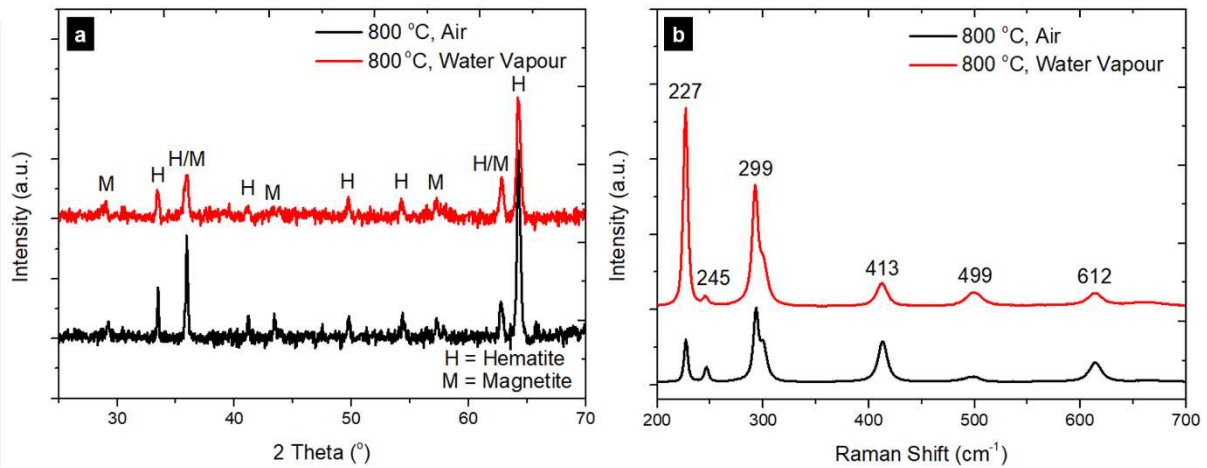
157 Fig. 4. (a) HR-TEM image of a single α -Fe₂O₃ NW and (b) FESEM image of iron foil oxidized at 800°C for 2
158 h in water vapor.

159

160 3.2 Crystal phase of the α -Fe₂O₃ NWs

161 Fig. 5 (a) presents XRD patterns of the iron foils oxidized at 800°C for 2 h in air and water vapor. The XRD
162 results indicated that the NWs consisted of crystalline structures with peaks indexed to hematite (α -Fe₂O₃) (ICDD
163 #98-001-2733) and magnetite (Fe₃O₄) (ICDD #98-001-7319). It has been previously reported that following the
164 thermal oxidation of iron, the outermost oxide layer is α -Fe₂O₃, and the underlying oxide is Fe₃O₄ (Yuan et al.
165 2012). To verify this, we performed Raman spectroscopy. The Raman results are presented in Fig. 5 (b) and
166 include bands at 227, 245, 293, 412, 499, and 612 cm⁻¹, which correspond to the α -Fe₂O₃ phase (Taniguchi et al.
167 2020). Owing to the low penetration depth of a Raman laser compared with XRD, we concluded that the outermost
168 oxide layer was α -Fe₂O₃. Also, although the water-vapor-assisted oxidation resulted in a denser formation of NWs,
169 the outer α -Fe₂O₃ phase oxide layer was observed in the air-oxidized samples.

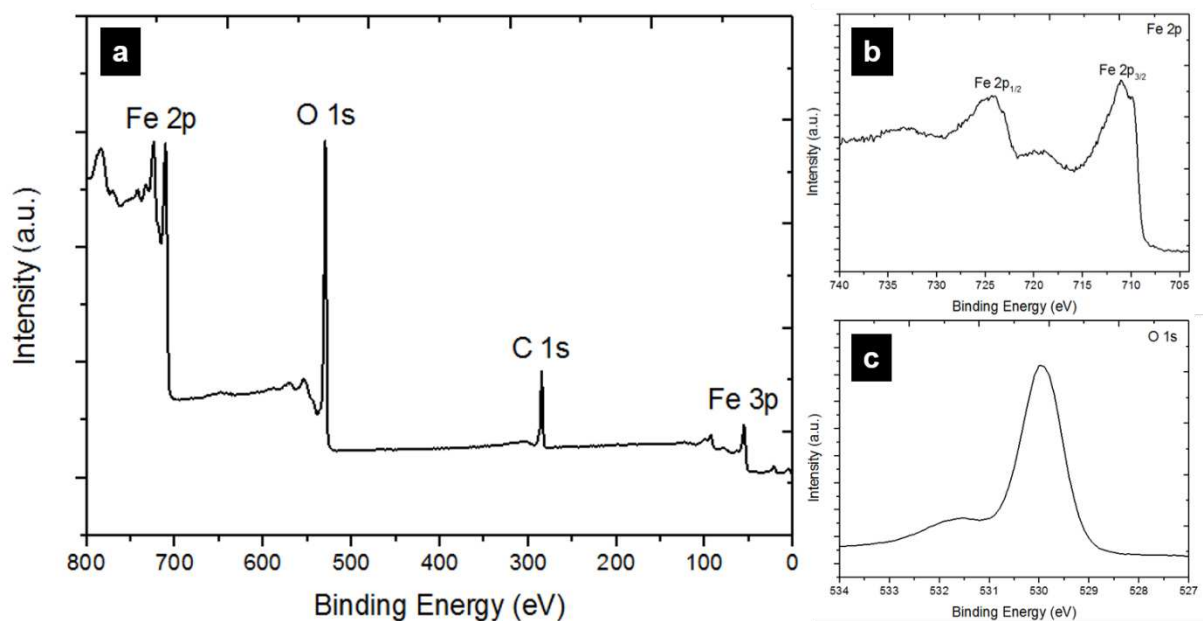
170



171
 172 Fig. 5. (a) XRD patterns and (b) Raman spectra of the iron foils oxidized at 800 °C for 2 h in air and water
 173 vapor.
 174

175 The surface elemental compositions of the foils oxidized at 800°C for 2 h in water vapor were confirmed
 176 using XPS measurements. The obtained XPS spectrum is presented Fig. 6 and indicates the presence of Fe, O,
 177 and C in the α -Fe₂O₃ NWs, as shown in the wide scan spectrum in Fig. 6 (a). Fig. 6 (b) presents a high-resolution
 178 spectrum of Fe 2p, including two peaks at 724.4 and 709.9 eV, which correspond to Fe 2p_{1/2} and Fe 2p_{3/2},
 179 respectively. A binding energy difference of 14.5 eV and the absence of a peak at 719.0 eV suggested a
 180 predominant Fe³⁺ oxidation state, which further verified the presence of the α -Fe₂O₃ phase (Ma et al. 2021). The
 181 O 1s peak, shown in Fig. 6 (c), with a binding energy of 530 eV corresponds to the O²⁻ oxidation state in the oxide,
 182 and the second broad peak at 531.5 eV corresponds to the adsorbed oxygen or hydroxyl ion (Ma et al. 2021).
 183 These XPS results further indicated that the outermost layer generated on the surface of the oxidized foils consisted
 184 of α -Fe₂O₃.

185



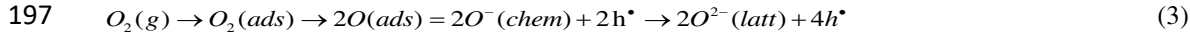
186
 187 Fig. 6. (a) Wide scan, (b) Fe 2p, and (c) O 1s XPS spectra of iron foils oxidized at 800°C in water vapor for 2
 188 h.

189

190 3.3 Growth mechanism of the NWs

191 3.3.1. Initial oxidation stage

192 During dry-air thermal oxidation, the diffusion process is initiated by the chemisorption of oxygen onto the
193 surface the iron foil, forming a chemisorbed layer, which is then followed by the ionization of oxygen, forming
194 O^{2-} (Eq. 3). The ionization of oxygen generates an electric field on the surface of the foil and triggers the oxidation
195 of Fe (Eq. 4). Overall, the reciprocal diffusion of oxygen and iron promotes the buildup of the oxide layer and
196 forms a thin layer of iron oxide.



199 During water-vapor-assisted thermal oxidation, the previously stable (Khanna 2002) (Eq. 5) adsorbed water
200 molecule dissociates as vapor (Eq. 5 and 6).



203 It has been reported that oxidation under water-vapor conditions is accelerated compared with in dry air [36],
204 which may be due to the incorporation of a proton, accompanied by electrons, within the oxide scale during oxide
205 growth. Fujii and Meussner reported that during oxidation in water vapor, the desorption of hydrogen from the
206 oxide surface occurred (Eq. 7); this resulted in partial dissolution in the oxide (Eq. 8) (Fujii and Meussner 1964).
207 The small ionic radius of H atoms compared with those of Fe and O (Lange 1985) means H can interstitially bind
208 with O as OH_o in the oxide. The creation of such defects, compensated by electron deficiency, metal vacancies,
209 and oxygen interstitials, may in turn increase the oxidation rate, resulting in the increased rate of NW formation
210 observed in this study.



213

214 3.3.2. Formation of the oxide scale

215 The interaction of iron with reactive oxidative gases at high temperatures resulted in the formation of an
216 oxide scale on the foil surface, as illustrated in the cross-sectional FESEM image in Fig. 7. This scale was
217 composed of multiple layers of oxides, an outer layer of α - Fe_2O_3 and an inner layer of $Fe_{1-x}O$ and Fe_3O_4 ,
218 depending on the oxidization temperature. $Fe_{1-x}O$ is thermodynamically unstable below 570°C; thus, it was likely
219 to be present during oxidation at the temperatures used in this study. The cross-sectional FESEM image in Fig. 7
220 indicates that the $Fe_{1-x}O$ layer was thicker than the Fe_3O_4 and α - Fe_2O_3 layers after oxidation at 800°C for 2 h
221 under water-vapor-assisted conditions. $Fe_{1-x}O$ is a non-stoichiometric compound with rich metal vacancies, which,
222 through phase transformation, aids the growth of other phases during oxidation. Phase formation is thought to
223 follow Eq. 9, with $Fe_{1-x}O$ being transformed first to Fe_3O_4 and then to α - Fe_2O_3 . The phase transformations during
224 oxidation in dry air and water vapor are presented in Table 1.



226

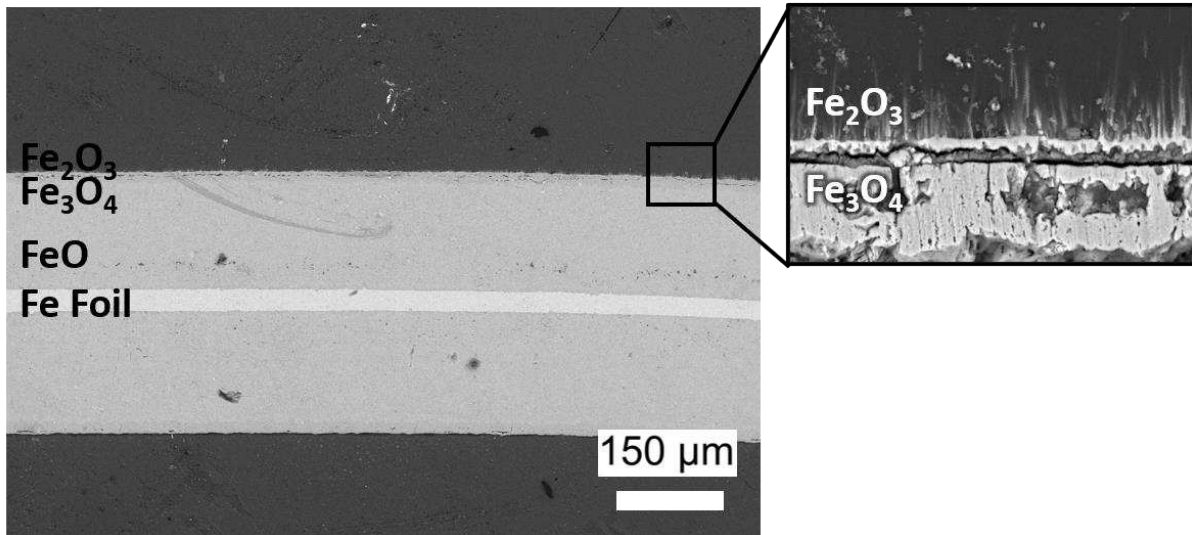


Fig. 7. Cross-sectional FESEM image of iron foils oxidized at 800 °C in water vapor for 2 h.

Table 1. Oxidation reactions of iron in dry and water-vapor-assisted conditions.

	Oxidation reaction in dry air	Oxidation reaction in water vapor
Air condition	$O_2 + 4e^- \rightarrow 2O^{2-}$	$H_2O \rightarrow OH_o^- + H_i^+$
Hematite (α - Fe_2O_3)	$2Fe^{3+} + 3O^{2-} \rightarrow Fe_2O_3$	$2Fe^{3+} + 3OH^- \rightarrow Fe_2O_3 + 3H^+$
Magnetite (Fe_3O_4)	$2Fe^{3+} + Fe^{2+} + 4O^{2-} \rightarrow Fe_3O_4$	$2Fe^{3+} + Fe^{2+} + 4OH^- \rightarrow Fe_3O_4 + 4H^+$
Wustite ($Fe_{1-x}O$)	$Fe^{2+} + O^{2-} \rightarrow FeO$	$Fe^{2+} + OH^- \rightarrow FeO + H^+$
Fe substrate	$Fe \rightarrow Fe^{2+} + 2e^-$	$Fe \rightarrow Fe^{2+} + 2e^-$

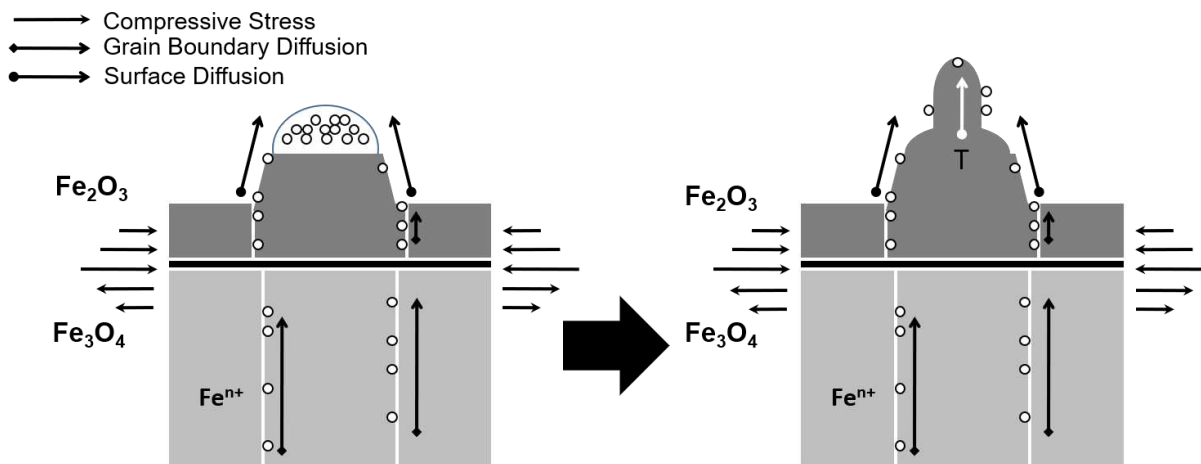
3.3.3. Oxidation growth stress

The cross-sectional FESEM images in Fig. 7 indicate that the surface region of the iron was composed of layered oxides in various phases, the presence of which generated stress within the oxide scale. During oxidation, thermal expansion leads to an increase in volume, which also contributes to oxide growth; however, this expansion resulted in a volume discrepancy of the iron and iron oxide, which induced a stress region at the metal–oxide interface. This caused the surface scale to be either in high compressive or tensile stress, especially at the interface regions; if the expansion of outer oxide layer is larger than that of the oxide layer underneath, a compressive stress develops (Pilling–Bedworth ratio > 1) in the upper oxide, and a tensile stress develops in the underlying oxide. This discrepancy alters the diffusion rate of the growing species, leading to preferential growth of the oxide at the oxide–air interface in the c-axis direction (Yuan et al. 2012).

The relaxation of the generated stresses resulted in the growth of NWs at the surface by a mechanism illustrated in Fig. 8. During the thermal oxidation process, Fe species diffuse and are accelerated across the oxide layer before nucleating on α - Fe_2O_3 grains through surface diffusion. This continuous and fast diffusion led to NW growth along the c-axis, which generated elongated oxide nanostructures, i.e., NWs. Observations under FESEM

247 evidenced this phenomena, with the nucleation and surface diffusion processes clearly seen in Figs. 9 (a) and (b),
 248 respectively.

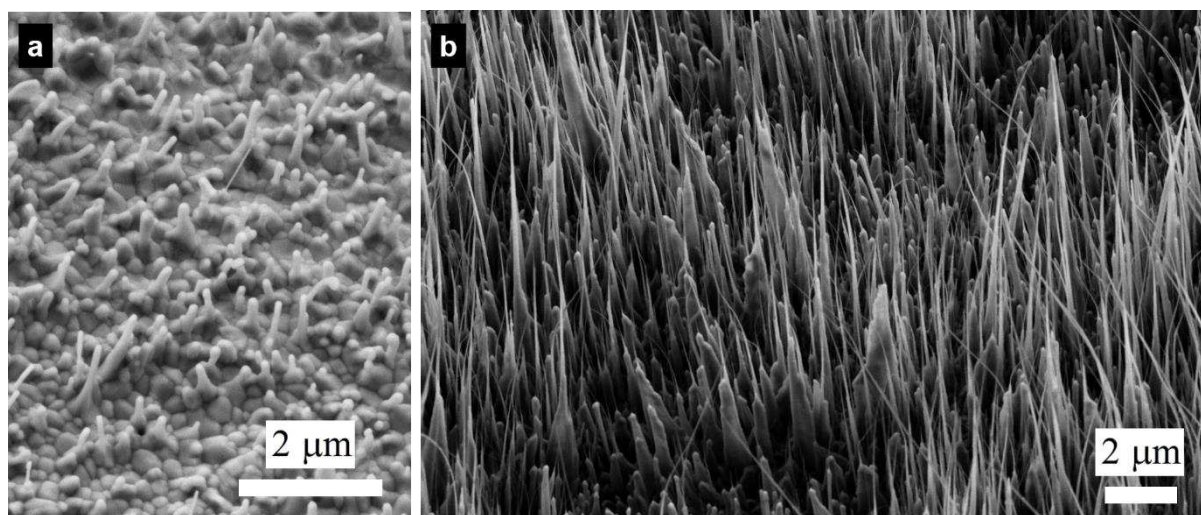
249



250

251 Fig. 8. Schematic illustration of the NW growth mechanism through thermal oxidation on an iron foil.

252



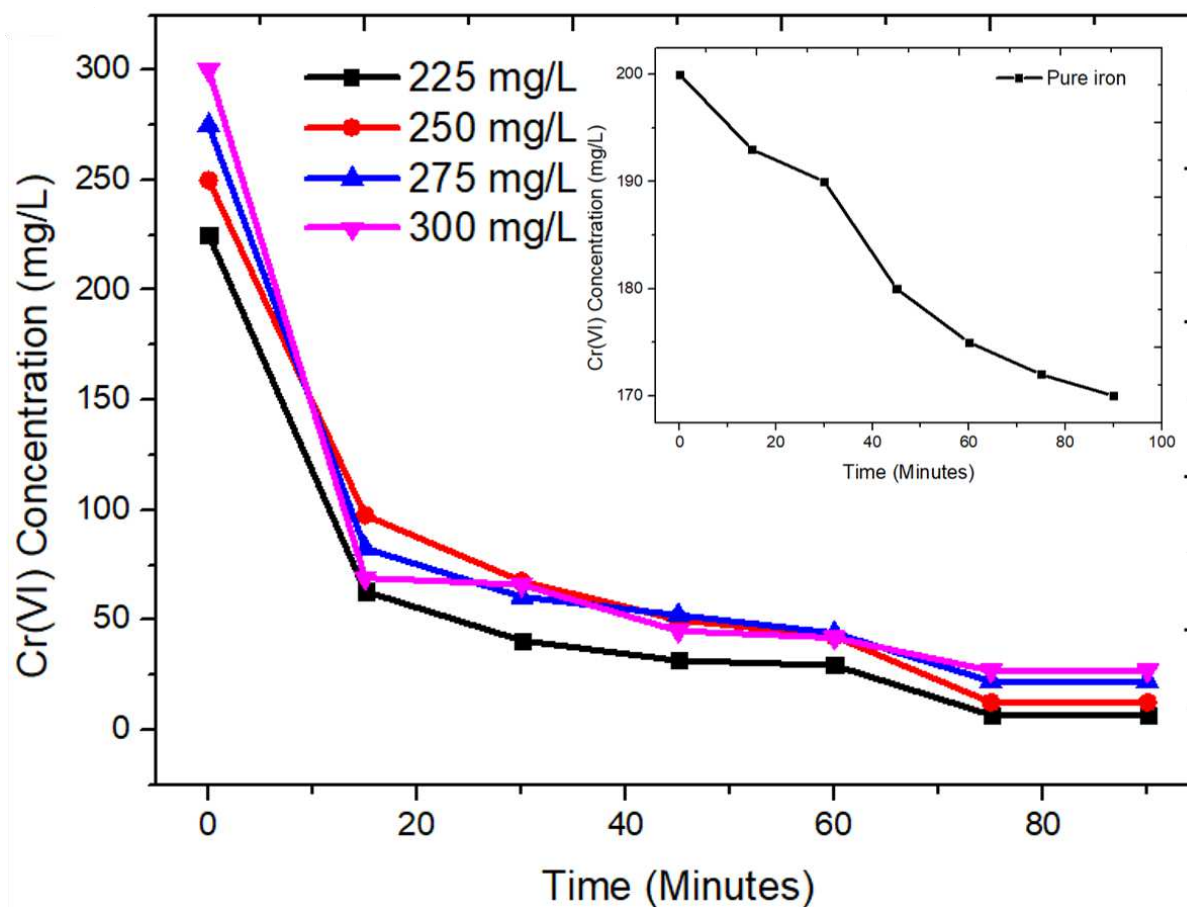
253

254 Fig. 9. FESEM image showing (a) the initial growth of NWs on α -Fe₂O₃ grains and (b) formation of NWs
 255 through surface diffusion.

256

257 3.4 Evaluation of Cr(VI) adsorption using the α -Fe₂O₃ NWs

258 We then evaluated the Cr(VI) adsorption properties of the NWs using the α -Fe₂O₃ NWs formed through
 259 thermal oxidation at 800°C for 2 h in water vapor, using various initial concentrations of Cr(VI) between 225 and
 260 300 mg/L. The results are illustrated in Fig. 10. The kinetic and equilibrium dynamics of the adsorption behavior
 261 were also obtained and evaluated. An equilibrium was reached after 90 min of contact between the NWs and the
 262 Cr(VI) solution, and the α -Fe₂O₃ NWs adsorbed of around 200 mg/L of Cr(VI) in a 50 ml solution. The adsorption
 263 profiles exhibited similar patterns across the various Cr(VI) solutions. A bare iron foil was used as a control using
 264 200 mg/L Cr(VI) solution, and the result is shown in the inset of Fig. 10. This demonstrated that the α -Fe₂O₃ NWs
 265 were required for more effective adsorption of Cr(VI).



266
 267 Fig. 10. Cr(VI) adsorption profiles from Cr(VI) solution concentrations between 225 and 300 mg/L using α -
 268 Fe_2O_3 NWs obtained from thermal oxidation at 800 °C in water vapor for 2 h. Inset is the Cr(VI) adsorption
 269 profile of a bare iron foil.
 270

271 As chromate ions exist as negative ions (HCrO_4^-) at pH 2 (Park et al. 2008), the surface charge of α - Fe_2O_3
 272 NWs must be positively charged for electrostatic attraction to happen. The immersion of the α - Fe_2O_3 NWs in a
 273 Cr(VI) solution starts a hydroxylation process, and the surfaces of the oxides are covered with hydroxyl ions
 274 (OH^-). The pH of the point of zero charge of α - Fe_2O_3 has been reported to be between pH 7.2 and pH 9.5 (Aredes
 275 et al. 2012), and because the pH used was below this, the surface of the NWs was protonated with H^+ ions, as
 276 shown in Eq. 10:



278 where S is the surface of the hydroxylated α - Fe_2O_3 NWs. Electrostatic interactions between Cr(VI) species and
 279 the positively charged α - Fe_2O_3 NW surfaces drove the adsorption process and the removal of Cr(VI) species from
 280 the solution (Nalbandian et al. 2016; Zhou et al. 2020).

281

282 3.5 Determination of adsorption kinetics

283 By knowing the rate of adsorption, we were able to investigate an appropriate kinetic model by fitting the
 284 data to several kinetic adsorption models: (1) pseudo-first-order, (2) pseudo-second-order, and (3) intraparticle
 285 diffusion, which are illustrated in Fig. 11. The validity of the predicted models with the experimental data was

286 determined using values of R^2 , which are presented in Table 2 along with the corresponding correlation
287 coefficients; the closer the value of R^2 to 1, the better the model fitted the adsorption kinetics of Cr(VI) in the
288 tested system. The details of the fitting of each model are described below.

289

290 3.5.1. Pseudo-first-order kinetic model

291 The linear fit of Cr(VI) adsorption on α -Fe₂O₃ NWs in accordance with a pseudo-first-order kinetic model
292 is presented in Fig. 11 (a). The pseudo-first-order model follows an adsorption process according to Eq. 11
293 (Largitte et al. 2016):

$$294 \frac{dq_t}{dt} = k(q_e - q_t). \quad (11)$$

295 By applying the initial condition, $q_t = 0$ at $t = 0$ and $q_t = q_t$ at $t = t$, the integration of the pseudo-first-order
296 model can be expressed as Eq. 12:

$$297 \log(q_e - q_t) = \log q_e - 0.434k_1t, \quad (12)$$

298 where q_e and q_t are the total adsorbed Cr(VI) at equilibrium and at time t (mg/g⁻¹), respectively, and k_1 is the
299 pseudo-first-order kinetic constant (min⁻¹). The R^2 values for the pseudo-first-order kinetic model in Table 2 are
300 below 0.8, indicating that the experimental data deviated from the theoretical data; therefore, this model was
301 unsuitable.

302

303 3.5.2. Pseudo-second-order kinetic model

304 The linear fit of Cr(VI) adsorption on α -Fe₂O₃ NWs according to the pseudo-second-order kinetic model is
305 presented in Fig. 11 (b). The pseudo-second-order kinetic model follows an adsorption process according to Eq.
306 13, which describes a kinetic rate driven by chemisorption (Largitte et al. 2016):

$$307 \frac{dq_t}{dt} = k_2(q_e - q_t)^2. \quad (13)$$

308 By applying the initial condition, $q_t = 0$ at $t = 0$ and $q_t = q_t$ at $t = t$, the integration of the pseudo-second-
309 order kinetic model can be expressed by Eq. 14:

$$310 \frac{t}{q_t} = \frac{1}{k_2q_e^2} + \frac{1}{q_e}t, \quad (14)$$

311 where q_e and q_t are the total adsorbed chromium at equilibrium and at time t (mg/g⁻¹), respectively. The
312 value of k_2 is the rate constant of pseudo-second-order adsorption (g/mg⁻¹/min). The R^2 values obtained for all the
313 concentrations investigated were higher than 0.98 for the pseudo-second-order model, as shown in Table 2,
314 indicating that it is appropriate to describe the dynamic behavior of Cr(VI) adsorption onto α -Fe₂O₃ NWs.

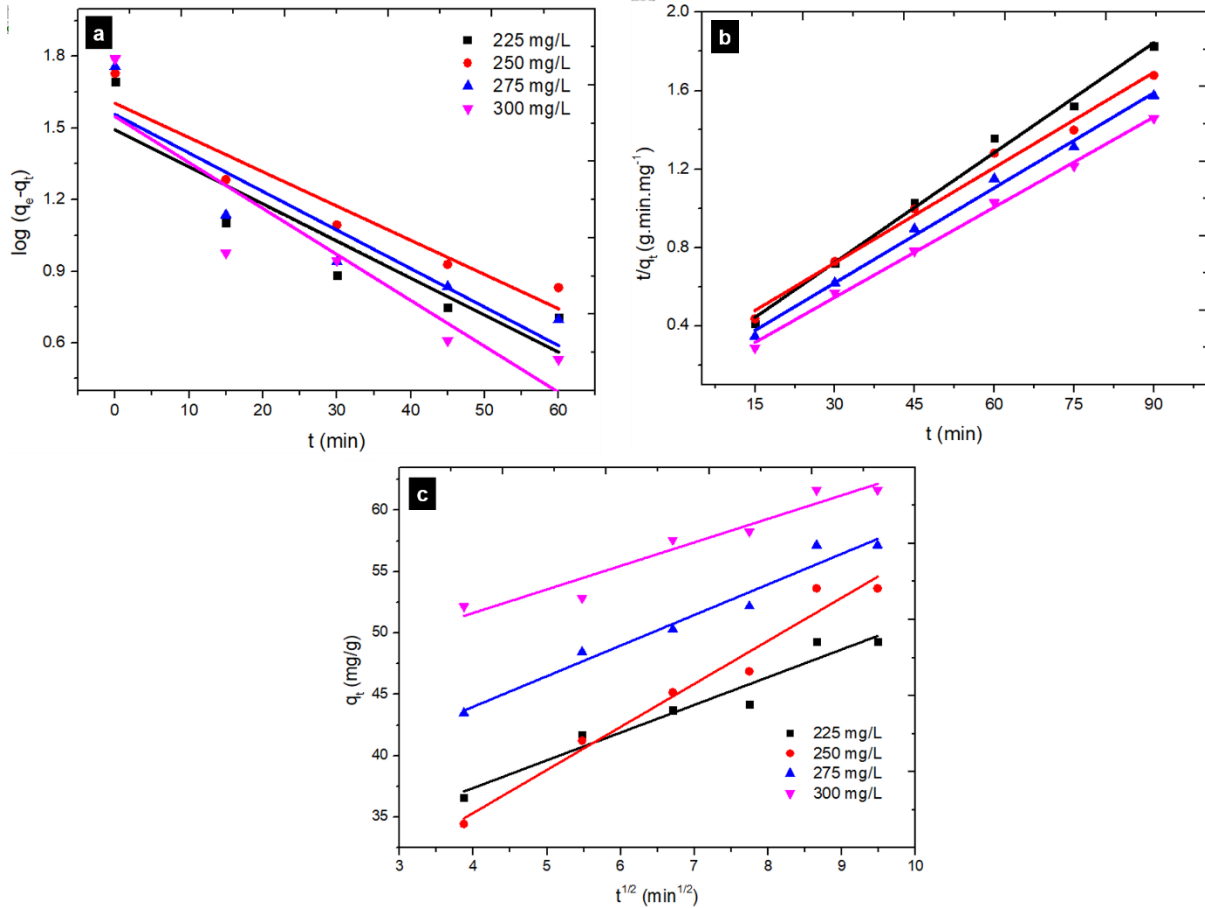
315

316 3.5.3. Intraparticle diffusion model

317 The linear fit of Cr(VI) adsorption on α -Fe₂O₃ NWs according to the intraparticle diffusion model is
318 presented in Fig. 11 (c). The intraparticle diffusion model describes an adsorption process that occurs in multiple
319 stages (Largitte et al. 2016). First, a sharp Cr(VI) concentration reduction indicates a spontaneous adsorption
320 process. Second, a gradual adsorption is driven by a controlled diffusion phenomenon. Finally, the low
321 concentration of the remaining adsorbate results in a slow adsorption process. The intraparticle diffusion model
322 can be expressed using Eq. 15:

323 $q_t = k_{id}(t)^{1/2} + c,$ (15)

324 where q_t (mg/g^{-1}) is the amount of Cr(VI) adsorbed, k_{id} is the rate factor ($\text{mg/g/min}^{1/2}$), and c (mg/g^{-1}) represents
 325 the boundary layer thickness. The R^2 values for the intraparticle diffusion model, presented in Table 2, were close
 326 to 0.9, which is even lower than the values obtained for the pseudo-second-order kinetic model. This indicated
 327 that the intraparticle diffusion model was unsuitable.
 328



329
 330 Fig. 11. Linear fit of $\alpha\text{-Fe}_2\text{O}_3$ NWs kinetics to (a) pseudo-first-order kinetic, (b) pseudo-second-order kinetic,
 331 and (c) intraparticle diffusion models.

332
 333 Table 2. Comparison of the kinetic models fitted for Cr(VI) adsorption.

Method	Sample	R^2	Kinetic rate constant
Pseudo-First Order	225 mg/L	0.77800	$k_1 = 0.03576$
	250 mg/L	0.88960	$k_1 = 0.03304$
	275 mg/L	0.80328	$k_1 = 0.03719$
	300 mg/L	0.78220	$k_1 = 0.00443$
Pseudo-Second Order	225 mg/L	0.99159	$k_2 = 0.00214$
	250 mg/L	0.98664	$k_2 = 0.00111$
	275 mg/L	0.99300	$k_2 = 0.00194$
	300 mg/L	0.99692	$k_2 = 0.00027$

Intra-Particle Diffusion	225 mg/L	0.93541	$k_{id} = 2.25689$
	250 mg/L	0.91151	$k_{id} = 3.50526$
	275 mg/L	0.92915	$k_{id} = 2.49014$
	300 mg/L	0.91090	$k_{id} = 1.91565$

334

335

336 3.6 Investigation on the adsorption equilibrium

337 To determine the loading capacity of the adsorbent, we continued investigating the equilibrium. The
 338 adsorption data were fitted to Langmuir and Freundlich models, and the obtained plots are presented in Fig. 12.
 339 Similarly to the kinetics study, the validity was determined by R^2 values, i.e., the closer R^2 was to 1, the better the
 340 fit of the model. The correlation coefficient and R^2 value for each model are presented in Table 3. Each model is
 341 described below.

342

343 3.6.1. Langmuir model

344 The linear fit of Cr(VI) adsorption on α -Fe₂O₃ NWs according to the Langmuir model is presented in Fig.
 345 12 (a). The Langmuir model describes an adsorption process that occurs across a homogeneous adsorbent surface
 346 (Foo et al. 2010), which can be described by Eq. 16:

$$347 \frac{C_e}{q_e} = \frac{1}{K_L \cdot q_m} + \frac{1}{q_m} \cdot C_e, \quad (16)$$

348 where K_L (L/mg⁻¹) is the Langmuir equilibrium constant, and q_m (mg/g⁻¹) is the monolayer capacity, which
 349 indicates the available active sites per mass of sample where Cr(VI) could be adsorbed. The R^2 value for the
 350 Langmuir model was close to 0.99, indicating that it fitted the equilibrium behavior of Cr(VI) adsorption onto α -
 351 Fe₂O₃ NWs well. The calculated adsorption capacity of α -Fe₂O₃ NWs for Cr(VI) using the Langmuir model was
 352 approximately 66.2690 mg/g.

353

354 3.6.2. Freundlich model

355 The linear fit of Cr(VI) adsorption on α -Fe₂O₃ NWs according to the Freundlich model is presented in Fig.
 356 12 (b). The Freundlich model describes an adsorption process that occurs across a heterogeneous adsorbent surface
 357 (Foo et al. 2010), which can be described by Eq. 17:

$$358 \log q_e = \log K_F + \frac{1}{n} \cdot \log C_e, \quad (17)$$

359 where K_F (mg/g⁻¹) is the Freundlich constant, which describes the adsorption capacity, and $1/n$ is the heterogeneity
 360 factor. It can be seen from Table 3 that the R^2 value for Freundlich model was below 0.95, indicating that the
 361 experimental data deviated from the theoretical data; therefore, the Freundlich model was unsuitable.

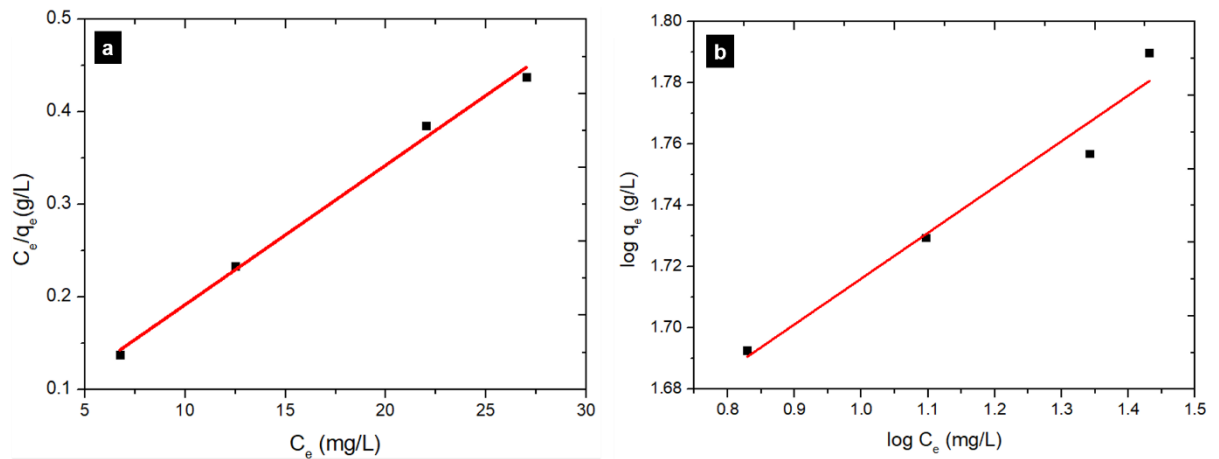


Fig. 12. Linear fit of Cr(VI) adsorption equilibrium to the (a) Langmuir and (b) Freundlich models.

Table 3. Summary of the adsorption equilibrium modeling.

Langmuir			Freundlich		
q_m (mg/g)	K_L	R^2	n	K_F	R^2
66.2690	0.37048	0.99209	6.68851	36.86888	0.94082

Finally, to demonstrate the impact of our findings, we compiled and compared previously reported Cr(VI) adsorption properties of iron oxide, presented in Table 4. This demonstrated that iron oxides can be used for Cr(VI) adsorption but that their adsorption properties differ depending on their morphologies. As previously mentioned, the adsorption capacity of Cr(VI) onto iron oxide is influenced by the pH of the solution, with a low pH being preferable to promote a higher adsorption capacity (Adegoke et al. 2013). Another factor that affects Cr(VI) adsorption is the specific surface area that is available for adsorption. Nalbandian et al. achieved an improved adsorption capacity of 90.9 mg/g using small-diameter (i.e., higher surface area) α -Fe₂O₃ nanofibers (Nalbandian et al. 2016). The TEM and SEM images in Figs. 2 and 4 allowed us to estimate the surface area provided by one NW to be approximately $204.28 \times 10^{-15} \text{ m}^2$. On a 1 cm \times 1 cm oxidized iron foil, we estimated there to be approximately 3×10^{10} NWs on the surface, assuming a homogeneous distribution; therefore, we consider our Cr(VI) adsorption capacity of 66.26 mg/g to be rather good. Although this is lower than the 1052.63 mg/g and 90.9 mg/g values reported by Kumar et al. (2019) and Nanbaldian et al. (2016), respectively, the use of α -Fe₂O₃ NWs on iron foils enables their simple removal from the target solution and improved recyclability. This indicates that the formation of α -Fe₂O₃ NWs by the water-vapor-assisted surface oxidation of iron has an excellent potential for the removal of harmful Cr(VI) from wastewater.

Table 4. Iron oxide Cr(VI) adsorption values from this study and the literature.

Iron oxide adsorbent material	pH	T (°C)	Adsorption capacity (mg/g)	References
Maghemite nanoparticles	2.5	25	19.2	(Hu et al. 2005)

3D hierarchical α-Fe₂O₃	3.0	25	34.4	(Liu et al. 2017)
α-Fe₂O₃ nanofibers	3.0	25	16.17	(Ren et al. 2013)
α-Fe₂O₃ nanoparticles	3.0	25	200	(Adegoke et al. 2013)
α-Fe₂O₃ nanofibers	6.0	25	90.9	(Nalbandian et al. 2016)
Fe³⁺ oxide/hydroxide NP	4.0	25	31.5	(Zelmanov and Semiat 2011)
Flower-like α-Fe₂O₃	3.0	25	7.6	(Cao et al. 2012)
Nanocrystalline iron oxide	2.0	25	2.29	(Gusain et al. 2016)
α-Fe₂O₃ nanostructure	2.0	25	22.72	Jia et al. 2013)
Iron oxide nanoparticles	5.2	25	1052.63	(Kumar et al. 2019)
α-Fe₂O₃ nanowires	2.0	25	66.26	This study

385

386 4. Conclusions

387 We investigated the high-temperature (700°C and 800°C) formation of iron oxide nanostructures through
388 thermal oxidation in dry-air- and water-vapor-assisted conditions. Oxidation at 700 °C led to the formation of
389 coral-like nanostructures, whereas α -Fe₂O₃ NWs were obtained from oxidation at 800 °C. Water-vapor-assisted
390 thermal oxidation resulted in an increased rate of oxide formation and larger or denser coral-like or NW structures
391 with high aspect ratios at 700 °C and 800 °C, respectively. Through systematically observing the oxidation process,
392 we were able to describe the formation mechanism of the α -Fe₂O₃ NWs, which was a stress-driven mechanism
393 through surface diffusion. Notably, NWs were produced after 5 min of oxidation, but the densest NWs with the
394 highest aspect ratio were obtained only after 2 h. We then evaluated the Cr(VI) adsorption property of α -Fe₂O₃
395 NWs obtained from water-vapor-assisted thermal oxidation at 800 °C for 2 h. A removal efficiency of 97% was
396 achieved within 90 min using an aqueous Cr(VI) solution with a concentration of 225 mg/L. Finally, we
397 investigated the adsorption equilibrium and kinetic models, which were in agreement with the Langmuir and
398 pseudo-second-order kinetic models, respectively. The adsorption capacity of these α -Fe₂O₃ NWs was calculated
399 to be 66.26 mg/g. This simple methodology for forming high-aspect-ratio α -Fe₂O₃ NWs through surface oxidation
400 has a great potential for producing large-surface-area adsorbents to enable the simple removal of Cr ions from
401 aqueous systems. The findings of this study will be beneficial and useful for the removal and mitigation of harmful
402 Cr(VI) ions from wastewater.

403

404

405 Acknowledgements

406 USM Research University Grant for Toyohashi University of Technology, Japan-USM collaboration
407 (1001/PBAHAN/870048) for Heavy Metal Mitigation. W. K. Tan acknowledges the JSPS KAKENHI Grant
408 Number JP18K14013 for supporting this research.

409

410 Ethical Approval

411 Not applicable.

412

413 Consent to Participate

414 Not applicable.

415

416 Consent for Publication

417 Not applicable.

418

419 **Authors Contributions**

420 Faisal Budiman: Investigation, Methodology, Writing-original draft. Wai Kian Tan: Investigation,
421 Visualization, Validation, Writing-Review and Editing, Funding acquisition. Go Kawamura: Validation. Hiroyuki
422 Muto: Validation. Atsunori Matsuda: Validation, Khairunisak Abdul Razak: Validation. Zainovia Lockman:
423 Conceptualization, Supervision, Writing-Review and Editing, Project Administration, Funding acquisition.

424 All authors read and approved the final manuscript.

425

426 **Funding**

427 USM Research University Grant for Toyohashi University of Technology, Japan-USM collaboration
428 (1001/PBAHAN/870048) for Heavy Metal Mitigation. JSPS KAKENHI Grant Number JP18K14013.

429

430 **Competing interests**

431 The authors declare that they have no completing interests.

432

433 **Availability of data and materials**

434 The datasets used and/or analysed during the current study are available from the corresponding author
435 on reasonable request.

436

437 **REFERENCES**

438 Abdullah N, Yusof N, Shah MHA, Ikhsan SNW, Ng ZC, Maji S, Lau WJ, Jaafar J, Ismail AF, Ariga K (2019)
439 Hydrous ferric oxide nanoparticles hosted porous polyethersulfone adsorptive membrane: chromium (VI)
440 adsorptive studies and its applicability for water/wastewater treatment. *Environ Sci Pollut Res* 26:20386-20399.
441 <https://doi.org/10.1007/s11356-019-05208-9>.

442 Adegoke HI, AmooAdekola F, Fatoki OS, Ximba BJ (2014) Adsorption of Cr (VI) on synthetic hematite (α -
443 Fe_2O_3) nanoparticles of different morphologies. *Korean J Chem Eng* 31:142-154.
444 <https://doi.org/10.1007/s11814-013-0204-7>.

445 Aquino CL, Balela MD (2020) Thermally grown Zn-doped hematite (α - Fe_2O_3) nanostructures for efficient
446 adsorption of Cr (VI) and Fenton-assisted degradation of methyl orange. *SN Appl. Sci.* 2:1-6.
447 <https://doi.org/10.1007/s42452-020-03950-1>.

448 Aredes S, Klein B, Pawlik M (2013) The removal of arsenic from water using natural iron oxide minerals. *J.*
449 *Clean. Prod.* 60:71-6. <https://doi.org/10.1016/j.jclepro.2012.10.035>.

450 Azeez NA, Dash SS, Gummedi SN, Deepa VS (2020) Nano-remediation of toxic heavy metal contamination:
451 Hexavalent chromium [Cr (VI)]. *Chemosphere.* 5:129204.

452 Bahmani P, Maleki A, Daraei H, Rezaee R, Khamforoush M, Athar SD, Gharibi F, Ziaee AH, McKay G (2019)
453 Application of modified electrospun nanofiber membranes with α - Fe_2O_3 nanoparticles in arsenate removal from
454 aqueous media. *Environ Sci Pollut Res* 26:21993-22009. <https://doi.org/10.1007/s11356-019-05228-5>.

455 Bashir N, Tan WK, Kawamura G, Matsuda A, Lockman Z. Comparison of ZrO_2 , TiO_2 , and α - Fe_2O_3
456 nanotube arrays on Cr (VI) photoreduction fabricated by anodization of Zr, Ti, and Fe foils. *Mater Res Express*
457 7:055013.

458 Bertrand N, Desgranges C, Poquillon D, Lafont MC, Monceau D (2010) Iron oxidation at low temperature
459 (260–500 °C) in air and the effect of water vapor. *Oxid Met* 73:139-162. [https://doi.org/10.1007/s11085-009-](https://doi.org/10.1007/s11085-009-9171-0)
460 9171-0.

461 Budiman F, Bashirov N, Tan WK, Razak KA, Matsuda A, Lockman Z (2016) Rapid nanosheets and nanowires
462 formation by thermal oxidation of iron in water vapour and their applications as Cr (VI) adsorbent. *Appl Surf*
463 *Sci* 380:172-177. <https://doi.org/10.1016/j.apsusc.2016.01.209>.

464 Cao CY, Qu J, Yan WS, Zhu JF, Wu ZY, Song WG (2012). Low-cost synthesis of flowerlike α -Fe₂O₃
465 nanostructures for heavy metal ion removal: adsorption property and mechanism. *Langmuir* 28:4573-4579.
466 <https://doi.org/10.1021/la300097y>.

467 Cornell RM, Schwertmann U (2003) *The iron oxides: structure, properties, reactions, occurrences and uses*.
468 John Wiley & Sons, New Jersey.

469 Deng J, Liu J, Dai H, Wang W (2018) Preparation of α -Fe₂O₃ nanowires through electrospinning and their
470 Ag₃PO₄ heterojunction composites with enhanced visible light photocatalytic activity. *Ferroelectrics* 528:58-65.
471 <https://doi.org/10.1080/00150193.2018.1448625>.

472 Fayazi M, Afzali D, Ghanei-Motlagh R, Iraj A (2019) Synthesis of novel sepiolite–iron oxide–manganese
473 dioxide nanocomposite and application for lead (II) removal from aqueous solutions. *Environ Sci Pollut Res*
474 26:18893-18903. <https://doi.org/10.1007/s11356-019-05119-9>.

475 Foo KY, Hameed BH (2010) Insights into the modeling of adsorption isotherm systems. *Chem Eng J* 156:2-10.
476 <https://doi.org/10.1016/j.cej.2009.09.013>.

477 Fu YY, Wang RM, Xu J, Chen J, Yan Y, Narlikar AV, Zhang H (2003) Synthesis of large arrays of aligned α -
478 Fe₂O₃ nanowires. *Chem. Phys. Lett.* 379:373-9. <https://doi.org/10.1016/j.cplett.2003.08.061>.

479 Fujii CT, Meussner RA (1964) The Mechanism of the High - Temperature Oxidation of Iron - Chromium
480 Alloys in Water Vapor. *J Electrochem* 111:1215. <https://doi.org/10.1149/1.2425963>.

481 Gao Z, Yang H, Fu X, Jin Q, Wu Q, Kang L, Wu J (2019) Efficient photoreduction of Cr (VI) on
482 TiO₂/functionalized activated carbon (TiO₂/AC-AEMP): improved adsorption of Cr (VI) and induced transfer of
483 electrons. *Environ Sci Pollut Res* 1-12. <https://doi.org/10.1007/s11356-019-05374-w>.

484 Guertin J, Avakian CP, Jacobs JA (2016) *Chromium (VI) handbook*. CRC press. Florida.

485 Gusain D, Srivastava V, Sillanpää M, Sharma YC (2016) Kinetics and isotherm study on adsorption of
486 chromium on nano crystalline iron oxide/hydroxide: linear and nonlinear analysis of isotherm and kinetic
487 parameters. *Res Chem Intermediat* 42:7133-7151. <https://doi.org/10.1007/s11164-016-2523-x>.

488 Hu J, Chen G, Lo IM (2005) Removal and recovery of Cr (VI) from wastewater by maghemite nanoparticles.
489 *Water Res* 39:4528-4536. <https://doi.org/10.1016/j.watres.2005.05.051>.

490 Jia Z, Wang Q, Ren D, Zhu R (2013) Fabrication of one-dimensional mesoporous α -Fe₂O₃ nanostructure via
491 self-sacrificial template and its enhanced Cr (VI) adsorption capacity. *Appl Surf Sci* 264:255-260.
492 <https://doi.org/10.1016/j.apsusc.2012.09.179>.

493 Khan FSA, Mubarak NM, Khalid M, Walvekar R, Abdullah EC, Mazari SA, Nizamuddin S, Karri RR (2020)
494 Magnetic nanoadsorbents' potential route for heavy metals removal—a review. *Environ Sci Pollut Res* 1-15.
495 <https://doi.org/10.1007/s11356-020-08711-6>.

496 Khanna AS (2002) *Introduction to high temperature oxidation and corrosion*. ASM international, Delhi.

497 Kumar H, Sinha SK, Goud VV, Das S (2019) Removal of Cr (VI) by magnetic iron oxide nanoparticles
 498 synthesized from extracellular polymeric substances of chromium resistant acid-tolerant bacterium
 499 *Lysinibacillus sphaericus* RTA-01. *J Environ Health Sci* 17:1-16. <https://doi.org/10.1007/s40201-019-00415-5>.

500 Lange NA D (1985) *Lange's Handbook of Chemistry*. McGraw-Hill, New York.

501 Largitte L, Pasquier R (2016) A review of the kinetics adsorption models and their application to the adsorption
 502 of lead by an activated carbon. *Chem Eng Res Des* 109:495-504. <https://doi.org/10.1016/j.cherd.2016.02.006>.

503 Lejding T, Engfeldt M, Bruze M, Isaksson M, Svedman C, Zimerson E, Verma K, Mowitz M (2020) Skin
 504 application of glutathione and iron sulfate can inhibit elicitation of allergic contact dermatitis from hexavalent
 505 chromium. *Contact dermatitis* 82:45-53. <https://doi.org/10.1111/cod.13409>

506 Lin CH, Lai CH, Peng YP, Wu PC, Chuang KY, Yen TY, Xiang YK (2019) Comparative health risk of inhaled
 507 exposure to organic solvents, toxic metals, and hexavalent chromium from the use of spray paints in Taiwan.
 508 *Environ Sci Pollut Res* 26:33906-33916. <https://doi.org/10.1007/s11356-018-2669-8>.

509 Liu Z, Yu R, Dong Y, Li W, Lv B (2017) The adsorption behavior and mechanism of Cr (VI) on 3D hierarchical
 510 α -Fe₂O₃ structures exposed by (0 0 1) and non-(0 0 1) planes. *Chem Eng J* 309:815-823.
 511 <https://doi.org/10.1016/j.cej.2016.10.108>.

512 Ma H, Hwang JB, Chae WS, Chung HS, Choi SH, Mahadik MA, Lee HH, Jang JS (2021). Magnetron
 513 sputtering strategy for Zr-Fe₂O₃ nanorod photoanode fabricated from ZrO_x/β-FeOOH nanorods for
 514 photoelectrochemical water splitting. *Appl. Surf. Sci* 30:149233. <https://doi.org/10.1016/j.apsusc.2021.149233>.

515 Nalbandian MJ, Zhang M, Sanchez J, Choa YH, Nam J, Cwiertny DM, Myung NV (2016) Synthesis and
 516 optimization of Fe₂O₃ nanofibers for chromate adsorption from contaminated water sources. *Chemosphere*
 517 144:975-981. <https://doi.org/10.1016/j.chemosphere.2015.08.056>.

518 Onchoke KK Sasu SA (2016) Determination of Hexavalent Chromium (Cr (VI)) concentrations via ion
 519 chromatography and UV-Vis spectrophotometry in samples collected from nacogdoches wastewater treatment
 520 plant, East Texas (USA). *Adv Environ Chem* 2016: 3468635. <https://doi.org/10.1155/2016/3468635>.

521 Park HJ, Tavlarides LL (2008) Adsorption of chromium (VI) from aqueous solutions using an imidazole
 522 functionalized adsorbent. *Ind Eng Chem Res* 47:3401-3409. <https://doi.org/10.1021/ie7017096>.

523 Ponti A, Raza MH, Pantò F, Ferretti AM, Triolo C, Patanè S, Pinna N, Santangelo S (2020) Structure, Defects,
 524 and Magnetism of Electrospun Hematite Nanofibers Silica-Coated by Atomic Layer Deposition. *Langmuir*
 525 36:1305-1319. <https://doi.org/10.1021/acs.langmuir.9b03587>.

526 Rahman Z, Singh VP (2019) The relative impact of toxic heavy metals (THMs)(arsenic (As), cadmium (Cd),
 527 chromium (Cr)(VI), mercury (Hg), and lead (Pb)) on the total environment: an overview. *Environ Monit Assess*
 528 191:419. <https://doi.org/10.1007/s10661-019-7528-7>.

529 Rahmat ST, Chin OY, Tan WK, Kawamura G, Matsuda A, Lockman Z (2018) Hierarchical Porous α -Fe₂O₃
 530 Formation by Thermal Oxidation of Iron as Catalyst for Cr (VI) Reduction. *IOP Conf Series: J Phys Conf Series*
 531 1082:012044. doi:10.1088/1742-6596/1082/1/012044.

532 Rahmat ST, Hong CY, Budiman F, Tan WK, Kawamura G, Matsuda A and Lockman Z (2018) Tailoring
 533 Parameters to Produce Nanowires on Metal Surface via Surface Oxidation Process. *IOP Conf Series: J Phys*
 534 *Conf Series* 1082: 012052. doi:10.1088/1742-6596/1082/1/012052.

535 Rahmat ST, Tan WK, Kawamura G, Matsuda A, Lockman Z (2020) Synthesis of rutile TiO₂ nanowires by
 536 thermal oxidation of titanium in the presence of KOH and their ability to photoreduce Cr (VI) ions. *J Alloys*
 537 *Compd* 812:152094. <https://doi.org/10.1016/j.jallcom.2019.152094>.

538 Rasheed A, Carvalho AAC, de Carvalho GGA, Ghous T, Nomura CS, Esposito, BP (2020) Chromium removal
539 from aqueous solutions using new silica gel conjugates of desferrioxamine or diethylenetriaminepentaacetic
540 acid. *Environ Sci Pollut Res* 27:1-10. <https://doi.org/10.1007/s11356-020-08097-5>.

541 Ren T, He P, Niu W, Wu Y, Ai L, Gou X (2013) Synthesis of α -Fe₂O₃ nanofibers for applications in removal
542 and recovery of Cr (VI) from wastewater. *Environ Sci Pollut Res* 20:155-162. <https://doi.org/10.1007/s11356-012-0842-z>

544 Rosli SA, Alias N, Bashrom N, Ismail S, Tan WK, Kawamura G, Matsuda A, Lockman Z (2021) Hexavalent
545 Chromium Removal via Photoreduction by Sunlight on Titanium–Dioxide Nanotubes Formed by Anodization
546 with a Fluorinated Glycerol–Water Electrolyte. *Catalysts* 11:376. <https://doi.org/10.3390/catal11030376>.

547 Singaraj SG, Mahanty B, Balachandran D, Padmaprabha A (2019) Adsorption and desorption of chromium with
548 humic acid coated iron oxide nanoparticles. *Environ Sci Pollut Res* 26:30044-30054.
549 <https://doi.org/10.1007/s11356-019-06164-0>.

550 Srivastava H, Srivastava AK, Babu M, Rai S, Ganguli T (2016) Topotaxial growth of α -Fe₂O₃ nanowires on
551 iron substrate in thermal annealing method. *J Appl Phys* 119:244311. <https://doi.org/10.1063/1.4954975>.

552 Sruthi PD, Sahithya CS, Justin C, SaiPriya C, Bhavya KS, Senthilkumar P, Samrot AV (2019) Utilization of
553 Chemically Synthesized Super Paramagnetic Iron Oxide Nanoparticles in Drug Delivery, Imaging and Heavy
554 Metal Removal. *J Clust Sci* 30:11-24. <https://doi.org/10.1007/s10876-018-1454-7>.

555 Sun X, Sun X, Liu X, Liu R, Li S, Shen M, Li Q (2020) One-dimensional Mg²⁺-induced α -Fe₂O₃ nanowires for
556 high-performance supercapacitor. *Results Mater* 5:100052. <https://doi.org/10.1016/j.rinma.2019.100052>.

557 Tan WK, Razak KA, Ibrahim K, Lockman Z (2011) Oxidation of etched Zn foil for the formation of ZnO
558 nanostructure. *J Alloys Compd* 509:6806-11. <https://doi.org/10.1016/j.jallcom.2011.03.055>.

559 Taniguchi K, Kitazawa N (2020) Characterization of α -Fe₂O₃ nanorod arrays prepared by a quasi-topotactic
560 transformation of solvothermal derived β -FeOOH nanowire-like arrays. *J Phys Chem Solids* 147:109632.
561 <https://doi.org/10.1016/j.jpcs.2020.109632>.

562 WHO G (2011) Guidelines for drinking-water quality. World Health Organization, Geneva.

563 Xie B, Shan C, Xu Z, Li X, Zhang X, Chen J, Pan B (2017) One-step removal of Cr (VI) at alkaline pH by
564 UV/sulfite process: reduction to Cr (III) and in situ Cr (III) precipitation. *Chem Eng J* 308:791-797.
565 <https://doi.org/10.1016/j.cej.2016.09.123>.

566 Yu JH, Lu JX, Smollin C, Cheng HT, Seak CJ, Chen HY (2020) N-acetylcysteine and ascorbic acid therapy for
567 acute hepatic injury after hexavalent chromium ingestion. *J Clin Pharm Ther* 45:208-210.
568 <https://doi.org/10.1111/jcpt.13044>.

569 Yuan L, Wang Y, Cai R, Jiang Q, Wang J, Li B, Sharma A, Zhou G (2012) The origin of hematite nanowire
570 growth during the thermal oxidation of iron. *Mat Sci Eng B* 177: 327-336.
571 <https://doi.org/10.1016/j.mseb.2011.12.034>.

572 Zelmanov G, Semiat R (2011) Iron (Fe⁺³) oxide/hydroxide nanoparticles-based agglomerates suspension as
573 adsorbent for chromium (Cr⁺⁶) removal from water and recovery. *Sep Purif Technol* 80:330-337.
574 <https://doi.org/10.1016/j.seppur.2011.05.016>.

575 Zhang R, Zeng Q, Guo P, Cui Y, Sun Y (2020) Efficient capture of Cr (VI) by carbon hollow fibers with
576 window-like structure. *Environ Sci Pollut Res* 27:1-11. <https://doi.org/10.1007/s11356-020-07939-6>.

577 Zheng Y, Yan Y, Yu L, Li H, Jiao B, Shiao Y, Li D (2020) Synergism of citric acid and zero-valent iron on Cr
578 (VI) removal from real contaminated soil by electrokinetic remediation. *Environ Sci Pollut Res* 27:5572-5583.
579 <https://doi.org/10.1007/s11356-019-06820-5>.

580 Zhou N, Gong K, Hu Q, Cheng X, Zhou J, Dong M, Wang N, Ding T, Qiu B, Guo Z (2020). Optimizing
581 nanocarbon shell in zero-valent iron nanoparticles for improved electron utilization in Cr (VI) reduction.
582 *Chemosphere* 42:125235. <https://doi.org/10.1016/j.chemosphere.2019.125235>.

583